

DETECTION OF IRON $K\alpha$ EMISSION FROM A COMPLETE SAMPLE OF SUBMILLIMETER GALAXIES

Robert R. Lindner¹, Andrew J. Baker¹, Alexandre Beelen², Frazer N. Owen³, and Maria Polletta⁴

ABSTRACT

We present an X-ray stacking analysis of a sample of 38 submillimeter galaxies with $\langle z \rangle = 2.6$ discovered at $\geq 4\sigma$ significance in the Lockman Hole North with the MAMBO array. We find a 5σ detection in the stacked soft band (0.5–2.0 keV) image, and no significant detection in the hard band (2.0–8 keV). We also perform rest-frame spectral stacking based on spectroscopic and photometric redshifts and find a $\sim 4\sigma$ detection of Fe $K\alpha$ emission with an equivalent width of $EW \gtrsim 1$ keV. The centroid of the Fe $K\alpha$ emission lies near 6.7 keV, indicating a possible contribution from highly ionized Fe XXV or Fe XXVI; there is also a slight indication that the line emission is more spatially extended than the X-ray continuum. This is the first X-ray analysis of a complete, flux-limited sample of SMGs with statistically robust radio counterparts.

Subject headings: Galaxies: Submillimeter, Galaxies: active, Galaxies: formation, X-rays: galaxies

1. Introduction

Submillimeter galaxies (SMGs) are distant star-forming systems with tremendous infrared luminosities ($L_{\text{IR}} [8\text{--}1000 \mu\text{m}] \gtrsim 10^{12} L_{\odot}$). In the (sub)millimeter waveband they are observable out to high redshifts due to the strong negative K -correction in the Rayleigh-Jeans regime of their thermal spectrum (see, e.g., Blain et al. 2002). The prevalence of SMGs at $z > 1$ (Chapman et al. 2005) in combination with their high rates of dust-obscured star-formation imply that they may be responsible for the production of a significant fraction of all the stellar mass in present-day galaxies. X-ray (Alexander et al. 2003, 2005b) and mid-infrared (Valiante et al. 2007; Menéndez-Delmeestre et al. 2007, 2009; Pope et al.

2008) spectroscopy shows that SMGs frequently contain active galactic nuclei (AGN) as well as powerful starbursts. This connection between star formation and accretion at high redshift may help explain the black hole mass-bulge mass relation in present-day galaxies (e.g., Alexander et al. 2005a). However, it remains hard to determine the relative importance of accretion and star formation for the SMG population as a whole because of the challenge of assembling large, statistically unbiased SMG samples.

Studying the X-ray properties of SMGs is difficult for two main reasons. First, the X-ray counterparts to SMGs are extremely faint. The count rate is so low that even the deepest *Chandra* and *XMM-Newton* spectra of SMGs cannot resolve features that serve as sensitive diagnostics of the physical conditions inside galaxies, like the Fe $K\alpha$ emission line. Fe $K\alpha$ emission is a ubiquitous feature in spectra of optically-selected AGN up to $z \simeq 3$ (e.g., Brusa et al. 2005; Chaudhary et al. 2010; Iwasawa et al. 2011), but the Fe $K\alpha$ emission properties of SMGs remain considerably more uncertain (Alexander et al. 2005b). Second, the requirement that SMGs need radio, (sub)millimeter, or mid-IR counterparts

¹Rutgers, The State University of New Jersey, 136 Frelinghuysen Road, Piscataway, NJ 08854-8019, USA; lindner@physics.rutgers.edu, ajbaker@physics.rutgers.edu

²Institut d’Astrophysique Spatiale, Université Paris Sud 11 and CNRS, Orsay, France; alexandre.beelen@ias.u-psud.fr

³National Radio Astronomy Observatory, P.O. Box O, Socorro, NM 87801, USA; fowen@nrao.edu

⁴INAF IASF Milano, via E. Bassini, 20133 Milan, Italy; polletta@iasf-milano.inaf.it

capable of nailing down their positions in high-resolution X-ray maps can lead to concessions of inhomogeneously-selected samples (e.g., including radio-selected galaxies; Alexander et al. 2005b), yielding results that conflict with X-ray studies of purely submillimeter-selected SMG samples (Laird et al. 2010; Georgantopoulos et al. 2011). To disentangle the relationship between SMGs and X-ray selected AGN, we need to overcome the uncertainty introduced by inhomogeneously selected samples, requiring X-ray spectral analyses of large, flux-limited samples of (sub)millimeter-selected SMGs with robust counterparts.

In this work, we report on an X-ray stacking analysis of a sample of 38 SMGs detected in a 1.2 mm map of the Lockman Hole North (LHN), one of the fields in the *Spitzer* Wide-Area Infrared Extragalactic (SWIRE) Survey (Lonsdale et al. 2003), using data from the *Chandra*-SWIRE survey (Polletta et al. 2006; Wilkes et al. 2009). The high radio counterpart identification rate of the LHN SMG sample (93%; Lindner et al. 2011) is afforded by the extremely deep 20 cm map of the same field (Owen & Morrison 2009), and allows for reliable X-ray photometry. The sample benefits from spectroscopic (Polletta et al. 2006; Owen & Morrison 2009; Fiolet et al. 2010) and optically-derived photometric (Strazzullo et al. 2010) redshifts. Additionally, analyses of *Herschel* observations of the LHN (Magdis et al. 2010; Roseboom et al. 2012) have delivered reliable photometric redshifts and infrared luminosities for a large fraction of the sample by fitting far-IR photometry with thermal-dust spectral energy distribution (SED) models.

In §2, we describe the observations used in our analysis. §3 outlines our X-ray stacking technique, and our method for deriving rest-frame luminosities. In §4, we compare our results to previous X-ray studies of SMGs, and discuss the possible origins of the FeK α emission seen in our stacked spectrum. In §5, we present our conclusions. In our calculations, we assume a *WMAP* cosmology with $H_0 = 70 \text{ km s}^{-1} \text{ Mpc}^{-1}$, $\Omega_M = 0.27$, and $\Omega_\lambda = 0.73$ (Komatsu et al. 2011).

2. Data and Sample Selection

2.1. Millimeter observations and stacking sample

Our SMG sample consists of 38 of the 41 significant detections in the 1.2 mm map (Lindner et al. 2011) of the LHN made using the Max Planck Millimeter Bolometer (MAMBO; Kreysa et al. 1998) array on the Institut de Radioastronomie Millimétrique 30 m telescope. We exclude one source that lacks a plausible 20 cm radio counterpart (L20), one that has a likely X-ray counterpart (L26), and one nearby galaxy at $z = 0.044$ (L29) from the stacking sample. Of our final sample of 38 galaxies, 37 (97%) have robust 20 cm radio counterparts with a chance of spurious association (P ; Downes et al. 1986) of $P < 0.05$; the remaining galaxy, L32, has $P = 0.056$. Stacking is performed with the coordinates of the SMGs' radio counterparts, which have a mean offset of $2.4''$ with respect to the SMG centroids. Five of our stacking targets have positions that are not listed in the 20 cm catalog of Owen & Morrison (2008) because they had $S/N < 5.0$ (L9, L28, and L36), or they were blended together with nearby radio sources (L17 and L39) during extraction (Owen & Morrison 2008; Lindner et al. 2011). The sample has a mean redshift of $\langle z \rangle = 2.6$ (see Table 1).

2.2. *Chandra* ACIS-I Observations

Our X-ray data are from the 3×3 -pointing raster mosaic of the LHN obtained with the Advanced CCD Imaging Spectrometer (ACIS-I; Weisskopf et al. 1996) on the *Chandra* X-ray telescope by Polletta et al. (2006). The final mosaic comprises nine 70 ks pointings arranged with $\sim 2'$ overlap (see Figure 1). It covers a total area of $\simeq 0.7 \text{ deg}^2$ and has a limiting conventional broad band (B_C ; 0.5-8.0 keV) sensitivity of $\sim 4 \times 10^{-16} \text{ erg s}^{-1} \text{ cm}^{-2}$ (Polletta et al. 2006). Fiolet et al. (2009) used these same data to search for a stacked X-ray signal among 33 *Spitzer* 24 μm -selected starburst galaxies, and found no significant 0.3–8 keV-band emission.

Within the sample of 41 MAMBO detections in the LHN, only L26 has a likely X-ray counterpart (CXOSWJ104523.6+585601) in the catalog of Wilkes et al. (2009). This X-

ray source has conventional broad band (B_C ; 0.5–8.0 keV), soft band (S_C ; 0.5–2.0 keV), and hard band (H_C ; 2.0–8.0 keV) X-ray fluxes of $f_{B_C} = 2.53 \times 10^{-15} \text{ erg s}^{-1} \text{ cm}^{-2}$, $f_{S_C} = 1.21 \times 10^{-15} \text{ erg s}^{-1} \text{ cm}^{-2}$, and $f_{H_C} = 1.57 \times 10^{-15} \text{ erg s}^{-1} \text{ cm}^{-2}$, respectively, and a hardness ratio of $\text{HR} = -0.32^{+0.31}_{-0.34}$. The hardness ratio is defined by $\text{HR} = (H_C - S_C)/(H_C + S_C)$, where H_C and S_C are the counts in the *Chandra* conventional hard and soft bands, respectively.

3. Stacking Analysis

In this section we describe our reduction of the *Chandra* X-ray data products and the methods used in our stacking analysis. We use two techniques: (1) image-based stacking in binned X-ray maps (§3.1), and (2) a photon-based spectral stacking procedure using optimized apertures (§3.2). The following subsections describe our implementation of these two methods.

3.1. Image-based stacking

We generate $1'' \times 1''$ -pixel gridded maps of the total counts and effective exposure time in the B_C , S_C , and H_C energy bands using the *Chandra* Interactive Analysis of Observations (CIAO; Fruscione et al. 2006) script `fluximage`. The characteristic energies input to `fluximage` to compute effective areas were 4.00 keV, 1.25 keV, and 5.00 keV for the B_C , S_C , and H_C bands, respectively. We then used the CIAO scripts `reproject_image` to merge the maps of each observation into one mosaic, and `dmimgcalc` to produce an exposure-corrected flux image in units of [photons $\text{cm}^{-2} \text{s}^{-1}$].

Figure 2 shows the resulting stacked image in each energy band. The $40'' \times 40''$ S/N postage stamp images are shown with a color stretch from $S/N = -4$ to $+4$. The peak S/N is 3.2, 4.8, and 2.0 in the B_C , S_C , and H_C bands, respectively. The peak of the strong stacked detection in the S_C band has an offset from the mean radio counterpart centroid position of $\lesssim 1''$.

3.2. Optimized broad-band stacking

Our second stacking technique does not use a binned X-ray map. Instead, we compute the stacked count rate and flux by directly counting

photons at the stacking positions. The photometric aperture at each stacking location is derived using a technique similar to the optimized stacking algorithm presented in Treister et al. (2011, supplementary information).

The size and shape of the aperture at each stacking position is chosen to maximize the point-source S/N at that position on the ACIS-I chips. The apertures are constructed as follows. For each stacking position (shown in Figure 1), we (1) use the CIAO script `mkpsf` to generate a 2D image of the local *Chandra* PSF, (2) convolve this PSF with a Gaussian smoothing kernel (see below), and (3) find the enclosed-energy fraction (EEF) contour C_{EEF} that maximizes the S/N of the flux within the aperture. The area enclosed by this contour defines the aperture. Because Poisson noise from the X-ray background is stronger than the flux at each position and the average exposure time does not change rapidly with increasing aperture size, the S/N within the aperture can be parametrized by C_{EEF} as

$$S/N \propto \frac{\text{EEF}}{\sqrt{A(C_{\text{EEF}})}}, \quad (1)$$

where $A(C_{\text{EEF}})$ is the total area enclosed by the contour C_{EEF} . This expression is the same as that derived by Treister et al. (2011), except that instead of using only circular apertures, we allow for non-axisymmetric apertures that follow the local shape of the *Chandra* PSF.

We compensate for the change in shape of the *Chandra* PSF with photon energy by generating two optimal apertures at each stacking position, one for each energy band (i.e., for characteristic energies of 1.25 keV and 5 keV). Parts of the LHN *Chandra* mosaic were imaged multiple times due to the overlapping edges of the individual exposures (see Figure 1). For these positions we find the total effective aperture by maximizing Equation 1 using a linear combination of PSFs, one for each overlapping observation.

We broaden the local *Chandra* PSFs to accommodate photons that do not lie at the stacking centers due to intrinsic wavelength offsets in the galaxies and astrometric errors. Previous X-ray stacking analyses find the optimal aperture radius to be $\sigma = 1.25\text{--}3.0''$ (Lehmer et al. 2005; Georgantopoulos et al. 2011). We find similarly

that our broad band stacked S/N is maximized with a smoothing kernel radius $\sigma_{\text{kernel}} = 1.3''$ (see Figure 3), so we adopt this value for our subsequent broadband photometry. The smallest angular separation of any pair of stacking targets ($15''$ for L17 and L39) is larger than the maximum radial extent of the largest X-ray stacking aperture, so we can ignore the effects of X-ray blending within our sample.

The photons used for background subtraction are collected from arrays of large circular apertures positioned next to each stacking target position. The apertures are manually positioned to exclude any bright nearby X-ray sources that could contaminate the background estimate. To avoid possible systematic uncertainties associated with the background subtraction (see, e.g., Treister et al. 2011; Willott 2011), we do not impose any S/N-based clipping or additional filtering in the background regions.

Table 3 shows the average stacked count rate and energy flux per galaxy in the three broad energy bands. We find a significant stacked detection in the soft band, and no significant detection in the hard band. To convert the stacked count rate into energy flux, we used the web-based CIAO Portable Interactive Multi-Mission Simulator¹ (PIMMS- version 4.4; Cycle 5). The fluxes are corrected for Galactic absorption using the column density in the direction of the LHN center, $N_{\text{H}} = 6.6 \times 10^{19} \text{ cm}^{-2}$ (Stark et al. 1992). Our non-detection in the hard band leaves our calculation of the hardness ratio relatively unconstrained, $\text{HR} = -0.68^{+0.51}_{-0.32}$ (setting a limit on the photon index $\Gamma > 1.2$), although it is clear that our sample has a steeply declining photon spectrum characteristic of star-forming galaxies (e.g., Ranalli et al. 2012). This estimate of HR was made after subtracting out the count rate in the soft band that is due to the strong FeK α line (see §3.3), which is a $\sim 20\%$ contribution for $1.3''$ -broadened photometric apertures.

A high photon index of $\Gamma = 1.6$ ($\text{HR} \simeq -0.37$) is found by Laird et al. (2010), who stack on SCUBA-detected SMGs in the *Chandra* Deep Field North (CDF-N). An even steeper photon index of $\Gamma = 1.9$ ($\text{HR} \simeq -0.49$) is measured by Georgantopoulos et al. (2011), who stack on

LABOCA-detected SMGs in the Extended *Chandra* Deep Field South (ECDF-S). We have used values of $\Gamma = 1.6$ and $\Gamma = 1.9$ to compute the stacked flux in each energy band (e.g., see Table 3), although the difference between the two estimates is less than the Poisson uncertainty (see Table 3).

3.3. Optimized spectral stacking

In addition to stacked broad-band fluxes, we also calculate the observed-frame and rest-frame stacked count-rate spectra for our sample.

For each stacking target, we use redshift information in the following order of priority, subject to availability: (1) spectroscopic (Polletta et al. 2006; Owen & Morrison 2009; Fiolet et al. 2010), (2) *Herschel*-based photometric (Magdis et al. 2010; Roseboom et al. 2012), (3) *AA*-quality optical-based photometric (Strazzullo et al. 2010), and (4) millimeter/radio photometric estimated using the Carilli & Yun (1999) spectral index $\alpha_{850\mu\text{m}}^{20\text{cm}}$ technique (Lindner et al. 2011). The redshift distribution of our sample is shown in Figure 4.

We use a flat sum of the observed counts at each stacking-target position with no weighting factors. Although this technique gives more weight to the brightest members of the stack, it is necessary given that *none* of our stacking targets are individually detected and therefore S/N-based weights (used in, e.g., Treister et al. 2011) cannot be reliably assigned. For the rest-frame data, we separately coadd, blueshift, and bin the background photons to avoid creating artificial spectral features (see, e.g., Yaqoob 2006).

The uncertainty in the rest-frame energy of the photons ΔE_{rest} as a function of the observed photon energies E_{obs} due to the typical redshift error Δz is estimated by the equation

$$\Delta E_{\text{rest}} = E_{\text{obs}} \frac{\langle \Delta z \rangle}{1 + \langle z \rangle}. \quad (2)$$

This uncertainty is always larger than the energy resolution of the ACIS-I chips, so we set the rest-frame energy bin widths to match ΔE_{rest} (Equation 2) using our sample's average redshift $\langle z \rangle = 2.6$ and redshift uncertainty $\langle \Delta z \rangle = 0.4$ (see Table 2).

Figures 5 and 6 show the net observed and

¹<http://cxc.harvard.edu/toolkit/pimms.jsp>

rest-frame count-rate spectra for our SMG sample, respectively. The rest-frame spectrum contains a 4σ emission feature with a centroid near 6.7 keV, which we attribute to Fe K α line emission from a mixture of Fe ionization states including Fe XXV (see §5.1.3). It is apparent from this rest-frame spectrum that a significant fraction of the observed soft-band flux is due to the Fe K α emission line. If strong unresolved Fe K α emission is a common feature in the X-ray spectra of other SMG samples, it may artificially lower their measured HR values by inflating their observed soft-band fluxes.

To ensure our stacking signal is not the result of contamination from a few strong targets, we performed a bootstrapping Monte Carlo analysis to recover the probability distribution for the single 6.7 keV-energy bin ($\text{bin}_{6.7}$). The mean number of on-target counts in $\text{bin}_{6.7}$ is 16, while the mean number of background counts in the bin is 8. Figure 7 shows that the resulting distribution closely matches that of an ideal Poisson distribution with a mean of 16, confirming that our stacking signal is characteristic of the entire sample, not a few outliers.

3.4. Estimating L_X and $L_{\text{FeK}\alpha}$

The mean stacked *rest-frame* hard-band X-ray luminosity, L_{H_C} , of our sample is given by

$$\langle L_{H_C} \rangle = 4\pi f_{H_C} \langle d_L^2 \rangle, \quad (3)$$

where f_{H_C} is the stacked energy flux per galaxy inside the observed 0.56–2.22 keV energy band (the 2.0–8 keV energy band, redshifted by $\langle z \rangle = 2.6$), and d_L is the luminosity distance at the redshift of each stacking target. We convert the observed count rate to an energy flux using PIMMS. The resulting rest frame X-ray luminosity is $\langle L_{H_C} \rangle = (3.0 \pm 1.1) \times 10^{42} \text{ erg s}^{-1}$.

To estimate the equivalent width and line flux of the Fe K α feature, we assume that the line emission is contained only within the single elevated bin at 6.7 keV (see Figure 6) and estimate the local count-rate continuum around the Fe K α feature by averaging together the 8 bins between 3–9 keV (excluding the bin containing the line). This results in an equivalent width of $\text{EW} = 3.9 \pm 2.5 \text{ keV}$. Although the EW is relatively unconstrained, it is $> 1 \text{ keV}$ with 90% confidence. Using the nom-

inal equivalent width and Equation A7, we find a mean stacked Fe K α line flux of $\langle f_{\text{FeK}\alpha} \rangle \simeq 2.1 \times 10^{-17} \text{ erg cm}^{-2} \text{ s}^{-1}$, and a mean line luminosity $\langle L_{\text{FeK}\alpha} \rangle = (1.3 \pm 0.4) \times 10^{42} \text{ erg s}^{-1}$.

Figure 3 also shows that the S/N of the Fe K α signal only drops at a larger radius than the broad-band signal. If we interpret the X-ray continuum as originating from the galaxies' nuclear regions, then this relative offset between the Fe K α emission and the X-ray continuum indicates that the Fe K α photons in our sample are systematically offset from the galaxies' centers. By measuring the distance between the peaks of the two curves in Figure 3, we estimate the radial offset to be $\sim 1''$. For our computation of the Fe K α line luminosity, we adopt an aperture broadening kernel suited to maximize the S/N of the Fe K α emission line, $\sigma_{\text{kernel}} = 2.4''$.

We use a two-sample Kolmogorov-Smirnov (KS) test to determine the significance of the apparent angular extension of the Fe K α emission relative to the continuum emission. First, we compute the *Chandra* PSF at the location of each stacking target, then sample the PSFs at the positions of their respective collections of optimally-selected photons (see §3.3). The PSFs are peak-normalized and smoothed by an amount σ_{smooth} to reflect intrinsic wavelength offsets and astrometric errors in the photon positions. We then compare the cumulative distributions of the observed soft-band (0.5–2.0 keV) continuum photons (excluding those in the rest-frame Fe K α bin) and the rest-frame Fe K α photons using the two-sample KS test to determine with what confidence $1 - p$ (p is the KS test significance) we can rule out the null hypothesis that the two samples are drawn from a common distribution. When using all 38 stacking positions, we find a maximum confidence of $1 - p = 0.71$ at $\sigma_{\text{smooth}} = 0.5''$ (63 continuum counts and 15 Fe K α counts). When we use only the stacking positions that have ≥ 1 Fe K α photon, the maximum confidence occurs at the same value of σ_{smooth} but has a reduced $1 - p = 0.45$ (29 continuum counts and 15 Fe K α counts). Therefore, the extension in the Fe K α emission relative to the continuum emission indicated by Figure 3 is a $\gtrsim 1\sigma$ (71% confidence) effect, whose significance is limited primarily by the small number of Fe K α photons.

4. Obscuration and Star Formation Rate

Two galaxies in our sample have L_{IR} [8–1000 μm] estimated from Magdis et al. (2010), and 12 from Roseboom et al. (2012). For the remaining galaxies without SED fits, we estimate L_{IR} by scaling the SED from the nearby, bolometrically-star formation dominated ULIRG, Arp 220:

$$L_{\text{IR}} = L_{\text{IR}}^{\text{Arp220}} \left(\frac{S_{1.2\text{mm}}}{S_{\nu_0}^{\text{Arp220}}} \right) \left[\frac{d_L(z)}{d_L(z_0)} \right]^2 \left(\frac{1+z_0}{1+z} \right), \quad (4)$$

in terms of

$$\nu_0 = 1.2 \text{ mm} \times \left(\frac{1+z}{1+z_0} \right), \quad (5)$$

$L_{\text{IR}}^{\text{Arp220}} = 1.3 \times 10^{12} L_{\odot}$, the observed 1.2mm flux density $S_{1.2\text{mm}}$, luminosity distance d_L , target redshift z , and Arp 220 redshift $z_0 = 0.018$. The L_{IR} values for all stacking targets are presented in Table 1; the average value of our whole sample is

$$\langle L_{\text{IR}} \rangle = (2.4 \pm 0.2) \times 10^{46} \text{ erg s}^{-1}. \quad (6)$$

The mean 20 cm radio luminosity density $L_{20\text{cm}}$ is calculated using our sample’s redshift distribution and 20 cm flux densities (Owen & Morrison 2008; Lindner et al. 2011):

$$\langle L_{20\text{cm}} \rangle = (2.5 \pm 0.3) \times 10^{31} \text{ erg s}^{-1} \text{ Hz}^{-1}. \quad (7)$$

We estimate the average star formation rate in our sample using the scaling relations of Kennicutt (1998) in the infrared and Bell (2003) at radio wavelengths, giving $\text{SFR}_{\text{IR}} \simeq (1100 \pm 100) M_{\odot} \text{ yr}^{-1}$ and $\text{SFR}_{\text{radio}} \simeq (1400 \pm 200) M_{\odot} \text{ yr}^{-1}$, respectively. These values are consistent with each other, but greater than the estimate using the X-ray scaling relation from Vattakunnel et al. (2012), $\text{SFR}_X \sim (500 \pm 300) M_{\odot} \text{ yr}^{-1}$. All three scaling relations assume a Salpeter (1955) initial mass function with limiting masses of 0.1 and $100 M_{\odot}$. The SFR estimated using the X-ray luminosity may be low due to intrinsic absorption. We can derive a lower limit on the average absorbing column in our sample by computing how much obscuration is required to reduce the value of SFR_X from an intrinsic value consistent with SFR_{IR} and $\text{SFR}_{\text{radio}}$. In this case, we would require $N_{\text{H}} \sim 2.3 \times 10^{23} \text{ cm}^{-2}$ based

on our observed flux in the 0.55–2.77 keV band assuming $\Gamma = 1.6$ and using $\langle z \rangle = 2.6$. If we use this argument to estimate the *unabsorbed* X-ray luminosity, we find $\langle L_{\text{HC}} \rangle \simeq 9.2 \times 10^{42} \text{ erg s}^{-1}$.

5. DISCUSSION

5.1. Comparison to previous surveys

In this section, we compare our results to those of previous X-ray analyses of SMG samples from the CDFN (Alexander et al. 2005b; Laird et al. 2010) and the (E)CDF-S (Georgantopoulos et al. 2011).

5.1.1. Detection rate

With only one significant X-ray counterpart in the LHN, the Lindner et al. (2011) SMG sample has an X-ray detection rate of $2_{-2}^{+6}\%$. Alexander et al. (2005b) find a high X-ray detection rate of $85_{-20}^{+15}\%$ among SMGs and submillimeter-targeted radio galaxies (which constitute 70% of their sample) in the CDFN. Laird et al. (2010) find a lower detection rate of $45 \pm 8\%$ using their purely submillimeter-selected sample derived from the inhomogeneously covered SCUBA supermap (Borys et al. 2003). The LESS sample of Georgantopoulos et al. (2011) is also purely submillimeter-selected and has an X-ray detection rate of $11_{-3}^{+4}\%$. However, unlike the SCUBA supermap, the LESS survey is produced with a single observing mode, and with uniform coverage.

We can place these four surveys in a common framework if we ask what fraction of SMGs in each survey have X-ray counterparts above the X-ray detection threshold in the LHN. In this case, we find 11 of 20 ($55_{-13}^{+14}\%$) for Alexander et al. (2005b), 0 of 35 ($0_{-0}^{+7}\%$) for Laird et al. (2010), and 11 of 126 ($9_{-3}^{+3}\%$) for Georgantopoulos et al. (2011). The latter two are in agreement with our sample in the LHN. These results indicate that a lower X-ray detection rate may be more characteristic of strictly submillimeter-detected SMGs from surveys made with uniform coverage.

5.1.2. $L_{\text{FeK}\alpha}$ vs. L_{IR} vs. $L_{20\text{cm}}$

Figure 8 shows our sample’s average X-ray (corrected only for Galactic absorption), radio, and IR luminosities compared to those of other stacked SMG samples (Laird et al. 2010;

Georgantopoulos et al. 2011), individually X-ray-detected SMGs (Alexander et al. 2005b; Laird et al. 2010; Georgantopoulos et al. 2011), and nearby LIRGs and ULIRGs (sample drawn from Iwasawa et al. 2009). Where available, we use the L_{IR} value from Table A2 of Pope et al. (2006) for the SMGs from the CDFN. For the twelve SMGs in Alexander et al. (2005b) that are not in the catalog of Pope et al. (2006), we scale $L_{\text{FIR}} \rightarrow L_{\text{IR}}$ using the average conversion factor f for the eight SMGs common between the two samples, $f = 1.42$. The 870 μm -detected SMGs from the (E)CDF-S are plotted with $L_{\text{IR}} = 10\text{--}1000 \mu\text{m}$. The local LIRGs and ULIRGs from Iwasawa et al. (2009) also have their $L_{\text{FIR}}(40\text{--}400 \mu\text{m})$ estimates scaled by $f = 1.42$. We also show the total sample luminosity average for Laird et al. (2010), including the contribution from their stacked SMGs that were not individually detected in the X-ray. The average properties of our stacking sample are in agreement with the total luminosities of Laird et al. (2010).

Figures 8 and 9 also indicate the AGN classification of each galaxy. Galaxies whose mid-IR or X-ray spectral properties are consistent with emission produced entirely by star formation are plotted in red, while those requiring the presence of an AGN are shown in blue. Georgantopoulos et al. (2011) divide their sample by using a probabilistic approach; those galaxies requiring the presence of a torus-dust component in their mid-IR SED according to an F-test are categorized as AGN. Laird et al. (2010) and Alexander et al. (2005b) separate out the AGN based on the most favored model of their X-ray spectra according to the Cash (1979) statistic. The sample of Iwasawa et al. (2009) is divided based on hardness ratio.

The division between AGN and non-AGN systems can be roughly determined based on the X-ray scaling relations of purely star-forming galaxies in the local universe (Ranalli et al. 2003; Vattakunnel et al. 2012), shown as solid black lines. The average properties of our stacking sample lie very near the Ranalli et al. (2003) relation. Considering the substantial intrinsic scatter in the spectral classifications of the Laird et al. (2010) sample, our stacking sample also probably contains a substantial fraction of both star-formation-only and AGN-required systems.

5.1.3. Fe K α emission properties

The Fe K α photons in our stacking sample may be more spatially extended than the continuum photons by $\sim 1''$ (see §3.4). Extended and misaligned Fe K α emission has been observed in Arp 220 (Iwasawa et al. 2005) and NGC 1068 (Young et al. 2001). We may also be blending together the emission from multiple components of merging systems of which only one component has strong Fe K α emission (like, e.g., Arp 299; Ballo et al. 2004).

The bin width in our stacked rest-frame X-ray spectrum, which is set by the redshift uncertainties of our SMG sample, is larger than the rest energy separation between Fe K α emission from neutral and highly-ionized iron (0.3 keV); therefore, it is difficult to determine the average Fe ionization fraction in our sample. Close inspection of the photons near the rest-frame Fe K α line (see Figure 10) reveals a range of values between 6.4 keV–7.2 keV, with a local maximum at 6.7 keV. Given that the Fe line photons are contributed fairly evenly by the 38 targets in our stacking sample, and have been assigned to their bins based on a wide variety of redshift estimation techniques (spectroscopic, optical-photometric, *Herschel*-photometric, millimeter/radio-photometric), they are unlikely all to be systematically biased high or low. Therefore, a significant fraction of the detected Fe K α photons likely originate from the highly-ionized species of Fe XXV or Fe XXVI. However, the $\sim 10\%$ rest-frame uncertainty in the energy of each photon implies an uncertainty in the centroid of the line profile of $\sigma_{\text{centroid}} = (\text{FWHM})/(\text{SNR}) \simeq 398 \text{ eV}$, insufficient to determine the relative fractions of each ionization state with certainty.

Strong emission ($\text{EW} = 1.8 \pm 0.9$) from highly ionized Fe K α has been observed in the nearby ULIRG Arp 220 by Iwasawa et al. (2005) using *XMM-Newton*. Iwasawa et al. (2009) also find strong 6.7 keV emission ($\text{EW} = 0.9 \pm 0.3 \text{ keV}$) from the stacked spectrum of nearby ULIRGs (including Arp 220) that have no evidence of AGN emission (termed X-ray-quiet ULIRGs). Alexander et al. (2005b) detected strong ($\text{EW} \simeq 1 \text{ keV}$) Fe K α emission in the stacked SMG spectrum of the six SMGs in their sample with $N_H > 5 \times 10^{23} \text{ cm}^{-2}$, and find that the line cen-

troid is between 6.7 keV and 6.4 keV, indicating a substantial contribution from highly ionized gas.

In Figure 11 we compare the relation between $L_{K\alpha}$ and L_{IR} in our sample with those for other individual systems and stacked samples with measured Fe K α line luminosities and bolometrically dominant energy sources that are well understood. The dashed line represents a linear slope between $L_{K\alpha}$ and L_{IR} and has been normalized to NGC 1068, a nearby prototypical Seyfert II LIRG. Red symbols represent systems that do not have significant observed AGN bolometric contributions, like SMGs and local X-ray quiet ULIRGs; the blue symbols represent systems that have significant bolometric AGN contributions. Figure 11 shows that the relative Fe K α /infrared luminosity fraction, $L_{K\alpha}/L_{IR}$, increases with increasing L_{IR} . If the Fe K α emission is due to AGN activity, then this result may be in agreement with the observed trend that LIRGs/ULIRGs tend to be increasingly AGN-dominated with increasing L_{IR} (e.g., Tran et al. 2001).

5.2. Origin of the Fe K α emission

This section discusses three possible physical origins for the Fe K α emission detected in our stacked SMG sample: supernovae, galactic-scale winds, and AGNs. Because a significant fraction of our sample’s Fe K α emission likely originates from the highly-ionized species Fe XXV (see, e.g., Figure 10) and because evidence for highly-ionized Fe K α emission from other (U)LIRGs exists at both high (Alexander et al. 2005b) and low (e.g., Iwasawa et al. 2005) redshifts, the following sections focus on the origin of this high-ionization component.

5.2.1. Supernovae

Here we consider if the observed Fe K α feature can be attributed to X-ray luminous supernovae. X-ray observations of the supernova SN 1986J in the nearby spiral galaxy NGC 831 reveal strong hard-band emission and a significant 6.7 keV (EW \lesssim 500 eV) line (Houck et al. 1998). Supernova 1986J decayed in the 2–10 keV band as $\sim t^{-2}$ from 1991 to 1996. We will take a conservative approach and use only the luminosity information in this time interval for our calculation. Given the X-ray luminosity and decay

rate of SN 1986J (Houck et al. 1998), and assuming the star formation rate of our sample of order $SFR = 10^3 M_{\odot} \text{ yr}^{-1}$ giving a supernova rate of 10 SN yr^{-1} , we would expect ~ 50 X-ray luminous supernovae to be visible at any given time. The combined supernova X-ray luminosity is therefore $L_{HC,SNR} \simeq 10^{42} \text{ erg s}^{-1}$. Considering the fact that prior to 1991 SN 1986J was probably still dimming at a rate close to $\propto t^{-2}$, this calculation is an underestimate. Therefore, supernovae like 1986J can satisfy the bolometric requirements for explaining the hard X-ray emission *and* the Fe K α line that we see in our stacked SMG sample.

However, if the supernovae associated with massive star formation are visible, then so must be high-mass X-ray binaries given the short time lifetimes of massive stars. These systems would dominate the hard X-ray emission from star-forming regions, and would severely dilute the Fe K α emission (see, e.g., Iwasawa et al. 2009). We therefore rule out X-ray luminous supernovae and supernova remnants as the source of the Fe K emission in our sample.

5.2.2. Galactic-scale winds

As discussed in Iwasawa et al. (2005), who consider the 6.7 keV emission line in Arp 220, a starburst-driven galactic-scale superwind of hot gas is energetically plausible as the source of the Fe K α emission. Large outflows could also explain why the Fe K α line emission appears more extended than the X-ray continuum emission in our stacking sample. To explore this scenario, we used the X-ray spectral-fitting package XSPEC (Arnaud 1996) to model an absorbed diffuse thermal X-ray (`zphabs * mekal`) spectrum and estimate the gas metallicity required to produce the strong high-ionization Fe K α emission detected in our SMG sample. We computed the model EW values using the spectral window 6.35–7.05 keV, the same energy width as the bin containing the Fe K α emission in our stacked rest-frame spectrum (Figure 6), which includes all Fe K α ionization states. We fixed the gas temperature to Arp 220’s best-fit value $kT = 7.4 \text{ keV}$ (Iwasawa et al. 2005), the gas density to $n = 1 \text{ cm}^{-3}$, the redshift to our sample’s average $\langle z \rangle = 2.6$, and the obscuring hydrogen column density to $2.3 \times 10^{23} \text{ cm}^{-2}$ (§4). Both the Fe K α line luminosity and the continuum intensity vary linearly with Z , allowing us to

express the relation between EW and Z as

$$\text{EW} = \frac{6.67}{1 + \frac{Z'}{Z}} \text{keV}, \quad (8)$$

where $Z' = 5.29 Z_{\odot}$. EW is approximately proportional to Z for $Z \ll Z'$ and approaches the constant value 6.67 keV for $Z \gg Z'$. Because of this non-linear behavior, an abundance of $0.94 Z_{\odot}$ can produce EW = 1 keV (90% confidence lower-limit) while a significantly greater abundance $Z \simeq 7.5 Z_{\odot}$ is needed to explain our nominal value EW $\simeq 3.9$ keV. If a significant amount of our rest-frame 2–10 keV luminosity is from X-ray binaries, incapable of generating the observed line emission, then the required metallicity would be even higher. While the lower limit on our measured EW can be explained by thermal emission from a diffuse ionized plasma, especially considering the extreme enrichment taking place in systems like SMGs, generating an EW with a value close to our nominal measurement would require an unrealistic degree of high- z enrichment.

5.2.3. AGN activity

AGNs hidden behind large hydrogen column densities may be responsible for the observed Fe K α emission in our sample. The Fe K α emission line is the signature spectral feature of the reprocessed (reflected) spectrum of an AGN (Matt et al. 2000). As the ionizing luminosity increases, so does the ionization fraction of the gas, shifting the dominant emission feature from 6.4 keV (neutral and intermediate ionization states) to 6.7 keV (helium-like Fe XXV) and 6.9 keV (hydrogen-like Fe XXVI).

Some insight into the properties of SMGs can be gained from reviewing the well-studied Fe K α emission properties of AGN and nearby ULIRGs. Strong (EW $\simeq 1$ keV) 6.7 keV emission has been observed in systems that are bolometrically AGN-dominated, like IRAS 00182-7112 (Nandra & Iwasawa 2007) and NGC 1068 (Young et al. 2001), as well as systems that appear to be energetically AGN-free, like Arp 220 (Iwasawa et al. 2005) and IC 694 (Ballo et al. 2004). However, direct evidence of a black hole accretion disk has been observed in Arp 220 by Downes & Eckart (2007) with the detection of a compact ($0.19'' \times 0.13''$) 1.3 mm continuum source in the center of the west nucleus torus. This source

has a surface luminosity of $\sim 5 \times 10^{14} L_{\odot} \text{kpc}^{-2}$, which is energetically incompatible with being powered by even the most extreme compact starbursts known. Only an accretion disk can be responsible for heating the dust. Highly ionized Fe K α emission has also been observed in the AGN systems Mrk 273 (Balestra et al. 2005), NGC 4945 (Done et al. 2003), and NGC 6240 (Boller et al. 2003), along with a neutral Fe K α component.

The narrow 6.4 keV “cold” Fe K α emission line is a ubiquitous feature in the spectra of optically-selected active galaxies out to high redshift (e.g., Corral et al. 2008; Iwasawa et al. 2011; Falocco et al. 2011). However, Iwasawa et al. (2011) also find evidence for highly ionized Fe K α emission in two subsets of their X-ray selected AGN sample: Type I AGN with the highest Eddington ratios, and Type II AGN with the highest redshifts. The subsamples with highly ionized K α emission show no evidence of a broad line Fe K α feature; therefore, the highly-ionized Fe K α photons probably do not originate from the accretion disk, but from more distant and tenuous outflowing gas. This scenario may also explain why the Fe K α photons in our sample appear spatially extended with respect to the X-ray continuum photons.

A significant caveat is that it remains difficult to reconcile the power source required to produce offsets as large as $1''$ in the photon distribution of our sample’s stacked Fe K α emission (relative to the nuclear continuum; see §3.4) given the sample’s low average X-ray luminosity. For example, we can calculate the maximum radial distance out to which low-density gas can remain highly photoionized by a single ionizing source by assuming that our sample’s stacked infrared luminosity is produced by deeply-buried AGNs, i.e., $L_{\text{ion}} \simeq L_{\text{IR}} = 2.4 \times 10^{46} \text{erg s}^{-1}$. Using the ionization parameter $\xi \equiv L_{\text{ion}}/nR^2$ ($\log \xi \geq 2.8$ is required for a significant Fe XXV ionization fraction: Kallman et al. 2004) with $n = 1 \text{cm}^{-3}$, we find $R_{\text{max}} = \sqrt{L_{\text{IR}}/n\xi} \simeq 2.0 \text{kpc}$. At our sample’s average redshift of $\langle z \rangle = 2.6$, this corresponds to a typical angular offset of $0.24''$. Angular offsets larger than $0.24''$, like those tentatively indicated by our sample (see Figure 3), can be explained by SMGs that host multiple distributed ionizing sources. In particular, the radio continuum emission (defining our stacking positions) might be

more closely associated with the X-ray continuum than with Fe K α line emission in a complex, multi-component system. These results highlight the importance of resolving the sizes and morphologies of SMGs with high-resolution (sub)millimeter imaging (e.g., Tacconi et al. 2006).

If the high-ionization Fe K α emission is ultimately due to star-formation processes (shocked gas from SNe), and the SFR is traced by the L_{IR} , then we should expect a linear relation between $L_{\text{K}\alpha}$ and L_{IR} . If the systems with the highest L_{IR} have an infrared contribution from obscured AGN that are not also emitting Fe K α photons, then we would expect a slope that is even less than unity. However, Figure 11 shows that $L_{\text{K}\alpha}$ is relatively much more dominant in SMGs and high- z AGN than in their lower-luminosity, lower-redshift analogues. This distinction indicates that highly ionized Fe K α emission cannot be explained solely by star-formation processes and is more likely to be the result of AGN activity.

6. Conclusions

We analyze the X-ray properties of a complete sample of SMGs with radio counterparts from the LHN. This sample's X-ray detection rate of $2^{+6}_{-2}\%$ is consistent with those for other uniformly-mapped, submillimeter-detected samples, considering the depth of our X-ray data. The X-ray undetected SMGs show a strong stacked detection in the S_C band, and no significant detection in the H_C band, similar to results from SMG stacking in the CDF-N (Laird et al. 2010) and CDF-S (Georgantopoulos et al. 2011).

We also use the available redshift information of our SMGs to compute the rest-frame, stacked count-rate spectrum of our sample. The rest-frame spectrum shows strong ($\text{EW} > 1 \text{ keV}$) emission from Fe K α , possibly with contributions from Fe XXV and Fe XXVI. A comparison with other high-ionization Fe K α -emitting systems from the literature indicates that accretion onto obscured AGNs is the likely explanation for the strong Fe K α emission line. In our sample, the Fe K α emission is responsible for $\sim 20\%$ of the observed soft-band X-ray flux. Therefore, if strong Fe line emission is a common feature in other SMG samples, it would significantly decrease the measured values of HR and lead to overestimates of the con-

tinuum spectral index Γ .

We find a tentative indication (71% confidence) that our sample's stacked distribution of Fe K α photons is more spatially extended than that of the X-ray continuum. If confirmed by future studies, this result can help determine the physical origin of the prominent Fe K α emission in SMGs.

We thank Jack Hughes, Dieter Lutz, and Alain Omont for useful discussions. We also thank the referee for useful comments that have improved the quality of this manuscript. This work has been supported by NSF grant AST-0708653, and has made use of the NASA/IPAC Extragalactic Database (NED) which is operated by the Jet Propulsion Laboratory, California Institute of Technology, under contract with the National Aeronautics and Space Administration.

Facilities: IRAM:30m, CXO.

A. Detailed descriptions of calculations

A.1. Optimized spectral stacking method

We begin by labeling all the photons within the optimized apertures (see Section 3.1) of all of the $N = 38$ stacking targets with the index i , and those within the background regions for the N targets i' . E_i is the energy of the i^{th} photon, and T_i is the total effective exposure time in the mosaic at the position of i . The notation $i \in j$ refers to all the photons that have energies located the j^{th} energy bin. The stacked mean count rate in the j^{th} energy bin, R_j , is then

$$R_j = \frac{1}{N} \sum_{i \in j} \frac{1}{T_i \kappa_i} \quad (\text{A1})$$

where κ_i is the aperture correction for the optimal aperture of the energy band of the i^{th} photon. The background mean count rate in the j^{th} bin is

$$R'_j = \frac{1}{N} \sum_{i' \in j} \frac{1}{T_{i'} \kappa_{i'} c_{i'}}, \quad (\text{A2})$$

where $c_{i'}$ is the ratio of the areas of the background region of the stacking position of the i'^{th} photon, and of the optimal aperture of that stacking position. It follows that the expected number of background counts in the j^{th} bin, \tilde{N}_j , is

$$\eta_j = \langle T_i \rangle_{i \in j} \times R'_j. \quad (\text{A3})$$

We use the double-sided 68%-confidence upper and lower limits, η_j^{high} , and η_j^{low} (Gehrels 1986), to compute the 1σ count rate deviations in the j^{th} bin due to the background, $\sigma^{\text{hi/low}}$:

$$\sigma_j^{\text{hi/low}} = \frac{|\eta_j^{\text{hi/low}} - \eta_j|}{\langle T_i \rangle_{i \in j}} \quad (\text{A4})$$

Therefore, the net count rate density per galaxy in the j^{th} bin, \mathbf{R}_j , is

$$\mathbf{R}_j = \frac{(R_j - \tilde{R}_j)^{+\sigma(R)_j^{\text{hi}}/\Delta E_j}}{\Delta E_j} \Big|_{-\sigma(R)_j^{\text{low}}/\Delta E_j} [\text{s}^{-1} \text{keV}^{-1}], \quad (\text{A5})$$

where ΔE_j is the width of the j^{th} energy bin. We calculate the corresponding rest-frame spectrum $\mathbf{R}_j^{\text{rest}}$ by binning the photons according to their rest-frame energies, $E_i^{\text{rest}} = E_i (1 + z_i)$, where z_i is the redshift of the stacking target associated with the photon.

A.2. Fe $K\alpha$ energy flux

We use the CIAO script `eff2evt` to tabulate the local effective area A_i ($A_{i'}$), and quantum efficiency Q_i ($Q_{i'}$), for each photon in the on-target (background) apertures.

The mean stacked on-target and background photon fluxes in the j^{th} bin, F_j , and F'_j , are then

$$F_j = \frac{1}{N} \sum_{i \in j} \frac{1}{T_i A_i Q_i \kappa_i}, \quad (\text{A6})$$

and

$$F'_j = \frac{1}{N} \sum_{i' \in j} \frac{1}{T_{i'} A_{i'} Q_{i'} \kappa_{i'} c_{i'}}, \quad (\text{A7})$$

respectively.

REFERENCES

- Alexander, D.M., Bauer, F. E., Brandt, W. N. et al. 2003, AJ, 125, 383
- Alexander, D. M., Smail, I., Bauer, F. E., et al. 2005, Nature, 434, 738
- Alexander, D. M., Bauer, F. E., Chapman, S. C., et al. 2005, ApJ, 632, 736
- Arnaud, K. A., 1996, Astronomical Data Analysis Software and Systems V, eds. Jacoby G. and Barnes J., p17, ASP Conf. Series Volume 101
- Balestra, I., Boller, Th., Gallo, L., Lutz, D., & Hess, S. 2005, A&A, 442, 469
- Ballo, L., Braitto, V., Della Ceca, R., et al. 2004, ApJ, 600, 634
- Barger, A., Cowie, L., Sanders, D., et al. 1998, Nature, 394, 248
- Barger, A. J., Cowie, L. L., Steffen, A. T., et al. 2001, ApJ, 560, L23
- Bell, E. F. 2003, ApJ, 586, 794
- Blain, A. W., Smail, I., Ivison, R. J., Kneib, J.P., & Frayer, T. 2002, Phys. Rep., 369, 111
- Boller, Th., Keil, R., Hasinger, G., et al. 2003, A&A, 411, 63
- Borys, C., Chapman, S., Halpern, M., & Scott, D. 2003, MNRAS, 344, 385
- Brandt, W. N., Alexander, D. M., Hornschemeier, A. E., et al. 2001, AJ, 122, 2810
- Brusa, M., Billi, R., & Comastri, A. 2005, ApJ, 621, L5
- Carilli, C. L., & Yun, M. S. 1999, ApJ, 513, L13
- Cash, W. 1979, ApJ, 228, 939
- Chaudhary, P., Brusa, M., Hasinger, G., Merloni, A., & Comastri, A. 2010, A&A, 518, A58
- Chapman, S. C., Blain, A. W., Smail, I., Ivison, R. J. 2005, ApJ, 622, 772
- Corral, A., Page, M. J., Carrera, F. J., et al. 2008, A&A, 492, 71
- Done, C., Madejski, G. M., Zycki, P. T., & Greenhill, L. J. 2003, ApJ, 588, 763
- Downes, A. J. B., Peacock, J. A., Savage, A., & Carrie, D. R. 1986, MNRAS, 218, 31
- Downes, D., & Eckart, A. 2007, A&A, 468, L57
- Falocco, S., Carrera, F., Corral, A., et al. 2012, A&A, 538, 83
- Fiolet, N., Omont, A., Polletta, M., et al. 2009, *Å*, 508, 117
- Fiolet, N., Omont, A., Lagache, G., et al. 2010, A&A, 524, A33
- Fruscione, A., McDowell, J. C., Allen, G. F., et al. 2006, Proc. SPIE, 6270, 62701V
- Gehrels, N. 1986, ApJ, 303, 336
- Georgantopoulos, I., Rovilos, E., & Comastri, A. 2011, A&A, 526, A46
- Holland, W. S., Robson, E. I., Gear, W. K., et al. 1999, MNRAS, 303, 659
- Houck, J., Bregman, J., Chevalier, R., & Tomisaka, K. 1998, ApJ, 493, 431
- Hughes, D. H., Serjeant, S., Dunlop, J., et al. 1998, Nature, 394, 241
- Iwasawa, K., Sanders, D. B., Evans, A. S., et al. 2005, MNRAS, 357, 565
- Iwasawa, K., Sanders, D. B., Evans, A. S., et al. 2009, ApJ, 695, L103
- Iwasawa, K., Sanders, D. B., Teng, S. H., et al. 2011, A&A, 529, A106
- Iwasawa, K., Mainieri, V., Brusa, M., et al. 2012, A&A, 537, 86
- Kallman, T. R., Palmeri, P., Bautista, M. A., Mendoza, C., & Krolik, J. H. 2004, ApJS, 155, 675
- Kennicutt, R. 1998, ARA&A, 36, 189
- Kreysa, E., Gemuend, H.-P., Gromke, J., et al. 1998, Proc. SPIE, 3357, 319
- Komatsu, E., Smith, K. M., Dunkley, J., et al. 2011, ApJS, 192, 18

- Laird, E. S., Nandra, K., Pope, A., & Scott, D. 2010, *MNRAS*, 401, 2763
- Lindner, R. R., Baker, A. J., Omont, A., et al. 2011, *ApJ*, 737, 83
- Lehmer, B. D., Brandt, W. N., Alexander, D. M., et al. 2005, *ApJ*, 129, 1
- Lonsdale, C. J., Smith, H., Rowan-Robinson, M., et al. 2003, *PASP*, 115, 897
- Magdis, G. E., Elbaz, D., Hwang, H., et al. 2010, *MNRAS*, 409, 22
- Matt, G., Fabian, A. C., Guainazzi, M., et al. 2000, *MNRAS*, 318, 173
- Menéndez-Delmeastre, K., Blain, A., Alexander, D., et al. 2007, *ApJ*, 655, L65
- Menéndez-Delmeastre, K., Blain, A., Smail, I., et al. 2009, *ApJ*, 699, 667
- Nandra, K., & Iwasawa, K. 2007, *MNRAS*, 382, L1
- Owen, F. N., & Morrison, G. E. 2008, *ApJ*, 136, 1889
- Owen, F. N., & Morrison, G. E., 2009, *ApJS*, 182, 625
- Ozawa, M., Koyama, K., Yamaguchi, H., Masai, K., & Tamagawa, T. 2009, *ApJ*, 706, L71
- Pilbratt, G. L., Riedinger, J. R., Passvogel, T., et al. 2010, *A&A*, 518, L1
- Polletta, M., Wilkes, B., Siana, B., et al. 2006, *ApJ*, 642, 673
- Pope, A., Scott, D., Dickinson, M., Chary, R.-R., et al. 2006, *MNRAS*, 370, 1185
- Pope, A., Chary, R.-R., Alexander, D., et al. 2008, *ApJ*, 675, 1171
- Ranalli, P., Comastri, A., & Setti, G. 2003, *A&A*, 399, 39
- Ranalli, P., Comastri, A., Zamorani, G., et al. 2012, *A&A*, 542, A16
- Roseboom, I. G., Ivison, R. J., Greve, T. R., et al. 2012, *MNRAS*, 419, 2758
- Salpeter, E. E. 1955, *ApJ*, 121, 161
- Sanders, D. B., Mazzarella, J. M., Kim, D.-C., Surace, J. A., & Soifer, B. T. 2003, *AJ*, 126, 1607
- Smail, I., Ivison, R., & Blain, A. 1997, *ApJ*, 490, L5
- Spergel, D. N., Bean, R., Doré, O., et al. 2007, *ApJS*, 170, 377
- Stark, A. A., Gammie, C. F., Wilson, R. W., et al. 1992, *ApJS*, 79, 77
- Strazzullo, V., Pannella, M., Owen, F. N., et al. 2010, *ApJ*, 714, 1305
- Tacconi, L., J., Neri, R., Chapman, S. C., et al. 2006, *ApJ*, 640, 228
- Teng, H., T. & Veilleux, S. 2010, *ApJ*, 725, 1848
- Tran, Q. D., Lutz, D., Genzel, R., et al. 2001, *ApJ*, 552, 527
- Treister, E., Schawinski, K., Volonteri, M., Natarajan, P., & Gawiser, E. 2011, *Nature*, 474, 356
- Valiante, E., Lutz, D., Sturm, E., et al. 2007, *ApJ*, 660, 1060
- Vattakunnel, S., Tozzi, P., Matteucci, F., et al. 2012, *MNRAS*, 420, 2190
- Wall, J. V., & Jenkins, C. R., 2003, Cambridge University Press, 130
- Wardlow, J. L., Smail, I., Coppin, K. E. K., et al. 2011, *MNRAS*, 415, 1479
- Wilkes, B. J., Kilgard, R., Kim, D.-W., et al. 2009, *ApJS*, 185, 433
- Willott, C. J. 2011, *ApJ*, 742, L8
- Weiss, A., Kovács, A., Coppin, K., et al. 2009, *ApJ*, 707, 1201
- Weisskopf, M. C., O'dell, S. L., & van Speybroeck, L. P. 1996, *Proc. SPIE*, 2805, 2
- Yaqoob, T. 2006, *Proceedings IAU Symposium No. 230*, 461
- Young, A. J., Wilson, A. S., & Shopbell P. L. 2001, *ApJ*, 556, 6

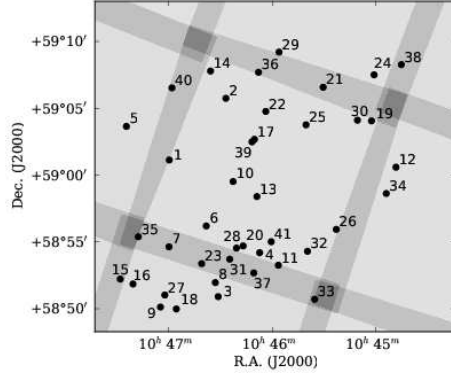


Fig. 1.— SMG positions inside the LHN. The filled circles mark the locations of the stacking targets used in this work and are labeled according to the SMGs' ID numbers from Table 1. The locations of the source without a reliable radio counterpart (L20), the nearby galaxy at $z = 0.044$ (L29), and the source with a likely X-ray counterpart (L26) are also shown even though they are not used in our stacking analysis. The greyscale image shows the relative *Chandra* effective exposure time across the field.

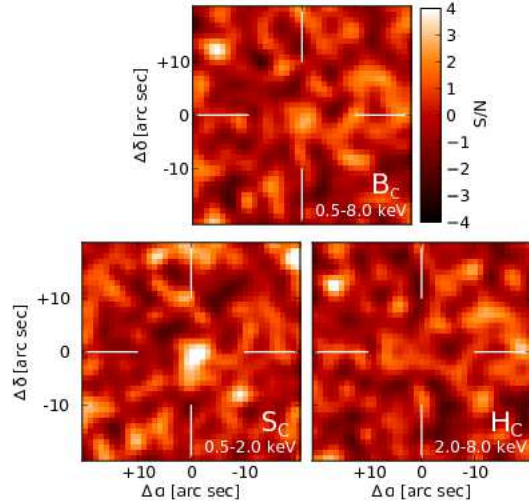


Fig. 2.— Stacked X-ray images showing the S/N in the B_C , H_C , and S_C *Chandra* energy bands. The white cross hairs mark the stacking center. The color stretch is $S/N=[-4,+4]$.

This 2-column preprint was prepared with the AAS L^AT_EX macros v5.2.

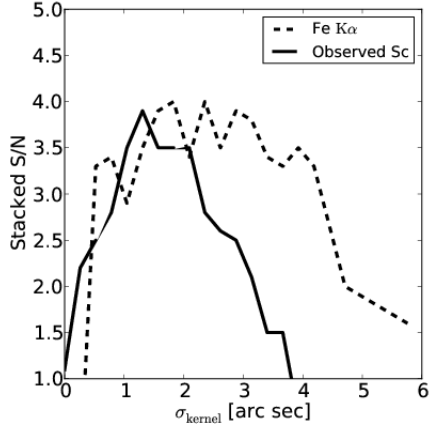


Fig. 3.— Stacked S/N of the observed S_C and rest-frame FeK α line fluxes as a function of the optimal aperture broadening kernel size σ_{kernel} .

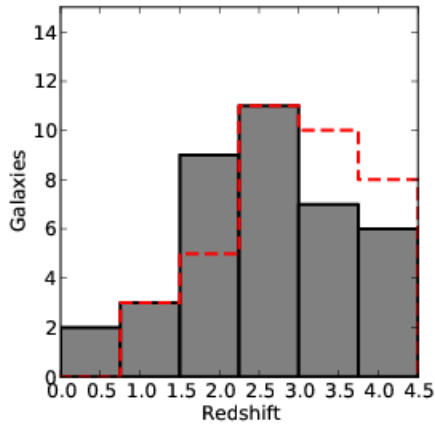


Fig. 4.— Redshift distribution for our sample of 38 SMGs. The filled histogram represents the redshifts used in this work, with $\langle z \rangle = 2.6$. The red dashed line represents the values as presented in Lindner et al. (2011), which relied more heavily on spectral index-based photometric redshifts.

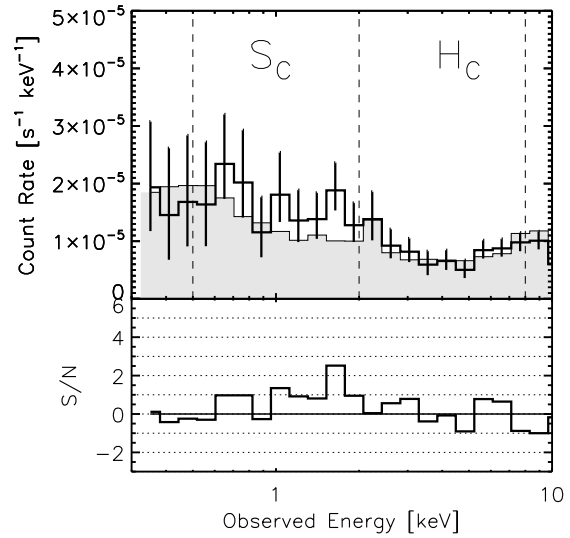


Fig. 5.— Stacked observed-frame X-ray spectrum of our SMG sample. *Above*: Count rate spectrum. The solid line and filled region represent the stacked on-target and background count rates. The error bars show the Poisson 68% double-sided confidence intervals due to the background. The dashed lines mark the extent of the S_C and H_C energy bands. *Below*: S/N of each bin in the above spectrum.

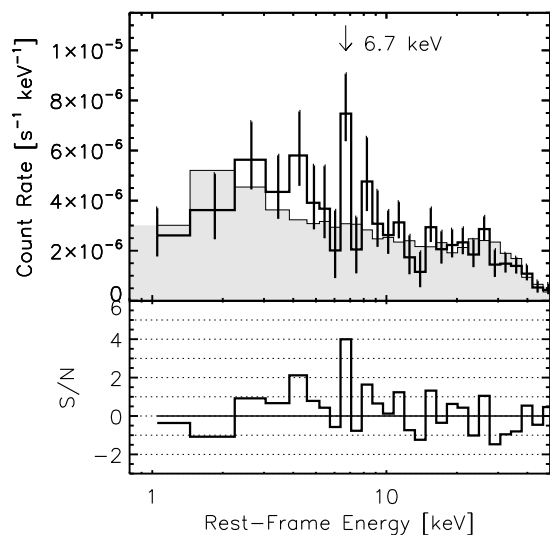


Fig. 6.— Stacked rest-frame X-ray spectrum of our SMG sample. *Above:* Count rate spectrum. The solid line and filled region represent the stacked on-target and background count rates. The error bars show the Poisson 68% double-sided confidence intervals due to the background only. The arrow marks the location of the rest-frame bin that is centered at 6.7 keV. *Below:* S/N of each bin in the above spectrum.

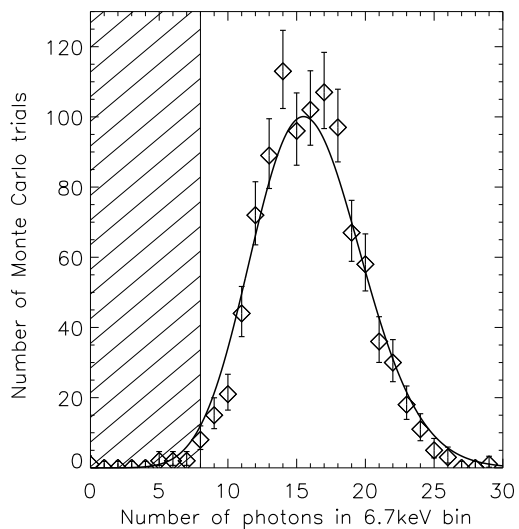


Fig. 7.— Bootstrap-Monte Carlo analysis of the number of FeK α counts in the 6.7 keV-bin of the rest-frame stacked spectrum (Figure 6). The histogram represents the total number of Monte Carlo trials returning the given number of total counts when randomly selecting 38 stacking positions from the original 38, with replacement. 16 counts lie in the 6.7 keV bin of the real data, and the mean Monte Carlo result is 15.9 counts. The solid curve shows an ideal Poisson distribution with mean $\mu = 16$. The shaded region represents the background level in this bin (8 counts).

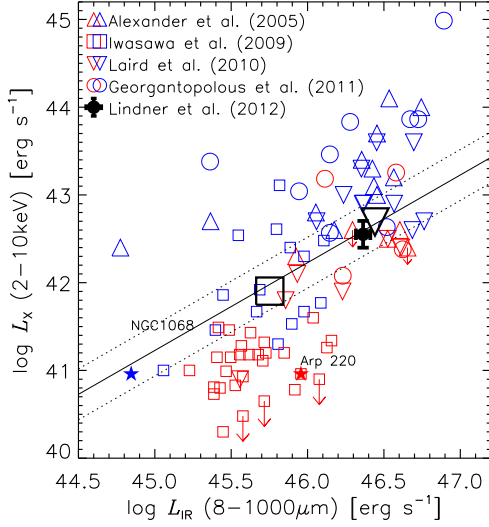


Fig. 8.— Log X-ray luminosity vs. log infrared (8–1000 μm) luminosity for our SMG sample compared to other stacked and individually detected SMGs, LIRGs, and ULIRGs from the literature: SMGs in the CDF-N from Alexander et al. (2005b, triangles) and Laird et al. (2010, upside-down triangles), SMGs in the ECDFS from Georgantopoulos et al. (2011, circles), and nearby LIRGs and ULIRGs from Iwasawa et al. (2009, squares). Red and blue symbols represent galaxies with “star formation-only” or “AGN-required” X-ray spectral classifications, respectively. The line represents the relation for star-forming galaxies in the local Universe (Ranalli et al. 2003). The black hollow symbols represent the average luminosities of all LIRGs/ULIRGs (Iwasawa et al. 2009, square), and all SMGs (including the stacked contribution) of the SCUBA supermap detections in the CDFN (Laird et al. 2010, upside-down triangle).

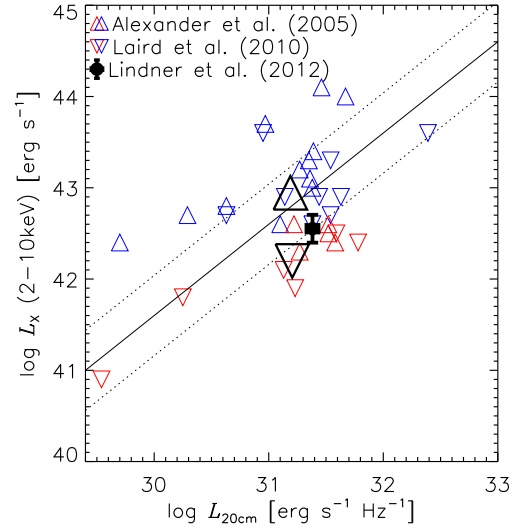


Fig. 9.— X-ray luminosity versus 20 cm spectral power. The symbols and colors are the same as in Figure 8. The over-plotted solid and dashed lines show the correlation between L_X and $L_{20\text{cm}}$ along with 1σ errors for star-forming galaxies (Vattakunnel et al. 2012).

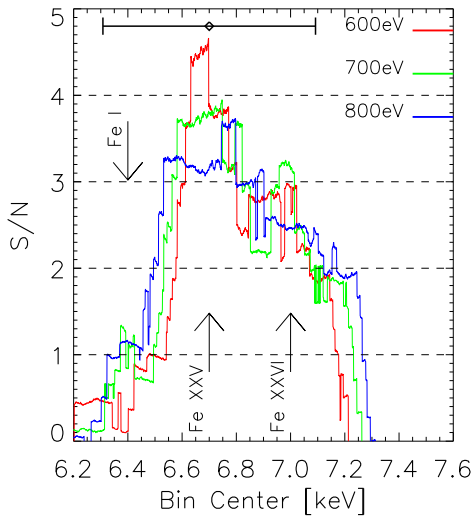


Fig. 10.— S/N of the FeK α emission as a function of bin position and width. The red, green, and blue lines use bin widths of 600 eV, 700 eV, and 800 eV (the bin width used in the rest frame spectrum in Figure 6 is 698 eV and is determined by the typical redshift uncertainty in our sample). The black arrows mark the energies of K α photons from Fe I (6.4 keV), Fe XXV (6.7 keV) and Fe XXVI (7.0 keV). The horizontal error bar shows the formal uncertainty in the line centroid $\sigma_{\text{centroid}} = \pm 398$ eV centered on 6.7 keV.

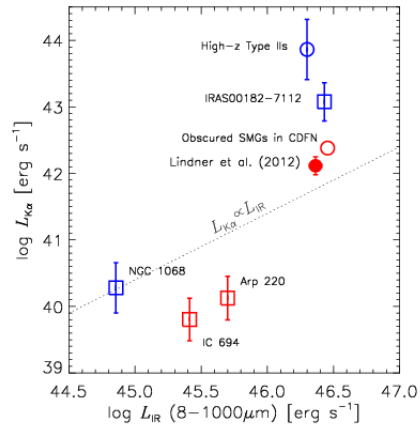


Fig. 11.— FeK α line luminosity $L_{K\alpha}$ versus L_{IR} for our results (filled red circle), stacked SMGs in the CDF-N (empty red circle; Alexander et al. 2005b), and stacked high- z Type II AGN (empty blue circle; Iwasawa et al. 2011). The squares represent the LIRG NGC 1068 (Young et al. 2001), the HyLIRG IRAS 00182-7112 (Nandra & Iwasawa 2007), and the merger component IC 694 (Ballo et al. 2004). The dashed line represents a linear relation that is normalized to NGC 1068. Blue (red) symbols denote samples/systems that do (do not) show strong AGN bolometric signatures.

TABLE 1
LHN MAMBO SMGs

ID	Name	RA ^a J2000	Dec ^a J2000	z	z type ^b	z reference ^c	$\log(L_{\text{IR}}/L_{\odot})^{\text{d}}$	L_{IR} reference ^c
L1	MM J104700.1 + 590109	161.75083	59.018778	2.562	S	P06	13.3	R12
L2	MM J104627.1 + 590546	161.61192	59.095778	4.09	P-IR	R12	12.9	L12
L3	MM J104631.4 + 585056	161.63112	58.848889	1.8	CY	L11	13.0	L12
L4	MM J104607.4 + 585413	161.53050	58.903889	4.4	CY	L11	12.7	L12
L5	MM J104725.2 + 590339	161.85592	59.060139	3.00	P-O	S10	13.1	R12
L6	MM J104638.4 + 585613	161.66112	58.936806	2.03	S	F10	12.9	R12
L7	MM J104700.1 + 585439	161.75054	58.911500	2.74	P-IR	R12	12.7	L12
L8	MM J104633.1 + 585159	161.63779	58.866417	2.07	P-IR	R12	12.8	L12
L9	MM J104704.9 + 585008	161.77071	58.835750	3.9	CY	L11	12.9	L12
L10	MM J104622.9 + 585933	161.59604	58.993000	3.01	P-IR	R12	12.7	L12
L11	MM J104556.5 + 585317	161.48721	58.888556	1.95	S	F10	12.9	R12
L12	MM J104448.0 + 590036	161.19829	59.009972	2.16	P-O	S10	12.7	R12
L13	MM J104609.0 + 585826	161.53646	58.974583	0.32	P-IR	R12	12.3	L12
L14	MM J104636.1 + 590749	161.64937	59.130139	2.26	P-IR	R12	12.9	R12
L15	MM J104728.3 + 585213	161.86654	58.870583	2.78	P-IR	R12	13.3	R12
L16	MM J104720.9 + 585151	161.83633	58.864722	3.24	P-IR	R12	12.8	L12
L17	MM J104610.4 + 590242	161.54383	59.045000	2.65	P-IR	R12	12.7	L12
L18	MM J104655.7 + 585000	161.73021	58.834444	2.15	P-IR	R12	12.9	L12
L19	MM J104502.1 + 590404	161.25833	59.067583	4.1	CY	L11	12.6	L12
L20	MM J104617.0 + 585444	161.57058	58.913694	> 4.6	CY	L11	–	–
L21	MM J104530.3 + 590636	161.37575	59.110083	2.52	P-IR	R12	12.6	L12
L22	MM J104603.8 + 590448	161.51763	59.080389	1.44	P-IR	R12	12.3	R12
L23	MM J104641.0 + 585324	161.67129	58.890500	3.6	CY	L11	12.6	L12
L24	MM J104500.5 + 590731	161.25279	59.126000	3.24	P-O	S10	12.7	R12
L25	MM J104540.3 + 590347	161.41679	59.063333	3.5	CY	L11	12.6	L12
L26	MM J104522.8 + 585558	161.34833	58.933611	> 5.0	CY	L11	–	–
L27	MM J104702.4 + 585102	161.76000	58.850861	1.62	P-IR	R12	12.7	L12
L28	MM J104620.9 + 585434	161.58804	58.909722	3.8	CY	L11	12.5	L12
L29	MM J104556.1 + 590914	161.48129	59.154528	0.044	S	O09	8.0	R12
L30	MM J104510.3 + 590408	161.29329	59.068639	0.71	P-IR	R12	12.5	L12
L31	MM J104624.7 + 585344	161.60379	58.896444	2.90	P-IR	R12	12.7	R12
L32	MM J104539.6 + 585419	161.41579	58.906917	2.40	P-IR	M10	12.57	M10
L33	MM J104535.5 + 585044	161.39608	58.847139	2.63	P-IR	R12	12.8	L12
L34	MM J104453.7 + 585838	161.22346	58.978194	2.46	P-IR	R12	12.6	L12
L35	MM J104717.9 + 585523	161.82546	58.923833	2.14	P-IR	R12	12.9	L12
L36	MM J104608.1 + 590744	161.53421	59.129444	4.5	CY	L11	12.5	L12
L37	MM J104610.8 + 585242	161.54575	58.879139	1.72	P-IR	M10	12.81	M10
L38	MM J104444.5 + 590817	161.18704	59.138361	3.6	CY	L11	12.5	L12
L39	MM J104611.9 + 590231	161.55012	59.042583	2.59	P-IR	R12	12.5	L12
L40	MM J104658.7 + 590633	161.74304	59.109306	0.78	P-IR	R12	12.5	L12
L41	MM J104600.7 + 585502	161.50129	58.917944	1.49	P-IR	R12	12.6	L12

^aPosition of 20 cm radio counterpart

^bRedshift type: S = spectroscopic, P-IR = *Herschel*-based photometric, P-O = optical-based photometric, CY = estimated using the spectral index $\alpha_{850\mu\text{m}}^{20\text{cm}}$ (Carilli & Yun 1999).

^cReferences: P06 = Polletta et al. (2006), O09 = Owen & Morrison (2009), F10 = Fiolet et al. (2010), M10 = Magdis et al. (2010), S10 = Strazzullo et al. (2010), L11 = Lindner et al. (2011), R12 = Roseboom et al. (2012), L12 = This Work

^d8–1000 μm

TABLE 2
REDSHIFT UNCERTAINTIES

Redshift type	N galaxies	Δz	References
Spectroscopic	3	$\simeq 0$	Polletta et al. (2006) Fiolet et al. (2010) Owen & Morrison (2009)
Optical-based photometric	3	0.2	Strazzullo et al. (2010)
Infrared-based photometric	23	0.4	Magdis et al. (2010) Roseboom et al. (2012)
Spectral index-based estimate (Carilli & Yun 1999)	9	0.6	Lindner et al. (2011)

TABLE 3
X-RAY STACKING RESULTS

Band	Energy keV	Net Rate 10^{-6} s^{-1}	Flux ($\Gamma = 1.6$) $10^{-17} \text{ erg cm}^{-2} \text{ s}^{-1}$	Flux ($\Gamma = 1.9$) $10^{-17} \text{ erg cm}^{-2} \text{ s}^{-1}$	L_X ($\Gamma = 1.6$) $10^{42} \text{ erg s}^{-1}$
S_C	0.5–2.0	$8.0^{+2.1}_{-2.0}$	$4.7^{+1.2}_{-1.2}$	$4.9^{+1.3}_{-1.2}$	–
H_C	2.0–8.0	$1.2^{+3.2}_{-2.9}$	< 9.7	< 9.1	–
B_C	0.5–8.0	$9.2^{+3.8}_{-3.5}$	$10.1^{+4.2}_{-3.9}$	$9.0^{+3.7}_{-3.4}$	–
H_C^{rest}	0.55–2.22	$8.0^{+2.1}_{-2.3}$	$4.8^{+1.3}_{-1.4}$	$4.9^{+1.3}_{-1.4}$	3.0 ± 1.1
H^{rest}	0.55–2.78	$8.6^{+2.4}_{-2.5}$	$5.7^{+1.6}_{-1.7}$	$5.7^{+1.6}_{-1.7}$	3.6 ± 1.3

NOTE.—Unabsorbed fluxes calculated assuming the given photon index with Galactic absorption only. Hydrogen column density taken as that of the central *Chandra* pointing, $N_H = 6.6 \times 10^{19} \text{ cm}^{-2}$ (Stark et al. 1992). Luminosity calculation uses $\Gamma = 1.6$.